Scilight

Bioinorganics and Biocatalysis
https://www.sciltp.com/journals/bb

Article

Green Peptide-Assisted Synthesis of Gold Nanoparticles for Electrochemical Biosensing of Carbamate Pesticides

Marcos R. de Araujo Silva [1], Barbara B. Gerbelli [2], Ana Cristina H. de Castro-Kochi [1,3], Andrea M. Aguilar [4] and Wendel A. Alves [1,*]

[1] Centro de Ciências Naturais e Humanas, Universidade Federal do ABC, Santo André 09280-560, Brazil
[2] Diamond Light Source, Didcot OX11 0DE, UK
[3] School of Biomedical Engineering, Einstein Hospital Israelita, São Paulo 05521-200, Brazil
[4] Instituto de Ciências Ambientais, Químicas e Farmacêuticas, Universidade Federal de São Paulo, Diadema 09972-270, Brazil
* Correspondence: wendel.alves@ufabc.edu.br

How To Cite: de Araujo Silva, M.R.; Gerbelli, B.B.; de Castro-Kochi, A.C.H.; et al. Green Peptide-Assisted Synthesis of Gold Nanoparticles for Electrochemical Biosensing of Carbamate Pesticides. *Bioinorganics and Biocatalysis* **2026**, *1*(1), 4.

Received: 31 October 2025
Revised: 18 December 2025
Accepted: 6 January 2026
Published: 16 January 2026

Abstract: Pest-control chemicals are widely used to increase agricultural productivity; however, their extensive application raises concerns regarding food safety, occupational health, and environmental contamination. Therefore, the development of efficient and reliable technologies for pesticide detection, particularly in environmental samples, remains a key research priority. In this study, an electrochemical biosensor based on square-wave voltammetry was developed by immobilizing acetylcholinesterase onto hydrothermally synthesized gold nanoparticles, using the cysteine–diphenylalanine (CFF) peptide as both a reducing and stabilizing agent. The CFF peptide enabled excellent morphological control of the gold nanostructures (hydrodynamic radius, 16 nm) and a uniform size distribution (polydispersity index, PDI = 0.322). Carbamate detection was performed by square-wave voltammetry, yielding a highly sensitive analytical response. The calibration curve exhibited a linear range up to 10^{-9} M, with a correlation coefficient (R^2) of 0.99 and a detection limit of 0.94 nM. The use of the CFF peptide and its self-assembling properties enabled the fabrication of an efficient and low-cost biosensor for carbamate detection, representing a promising approach for future environmental and agricultural monitoring applications.

Keywords: electrochemical biosensor; pesticide detection; gold nanoparticles; cysteine–diphenylalanine peptide; environmental monitoring

1. Introduction

The increasing global demand for food production has driven the intensive use of pesticides to control pests and weeds [1–4]. Among them, carbamates stand out for their effectiveness and relatively lower environmental persistence compared with organochlorine pesticides [5,6]. However, their mode of action—reversible inhibition of the enzyme acetylcholinesterase (AChE), which is essential for nerve impulse transmission—raises major concerns about environmental safety and human health [7,8]. The presence of these compounds in food and water supplies therefore represents a serious public health challenge, underscoring the urgent need for rapid, sensitive, and cost-effective detection methods [9].

Conventional analytical methods, such as high-performance liquid chromatography (HPLC) and gas chromatography, offer excellent sensitivity and selectivity but are limited by high operational costs, complex sample preparation requirements, and lengthy analysis times [10]. In this context, sensors and biosensors have emerged as attractive alternatives, enabling in situ analysis with high analytical performance, reduced costs, and

portability, which are particularly advantageous for applications in precision agriculture and real-time environmental monitoring [11].

Among the various strategies, electrochemical enzymatic biosensors have emerged as one of the most extensively explored approaches for detecting carbamates and organophosphates [12,13]. These devices exploit the catalytic inhibition of AChE by pesticides, correlating decreases in enzymatic activity with analyte concentration [14–16]. Different transduction modes have been employed, including potentiometric, amperometric, and conductometric systems, with amperometric biosensors being the most studied due to their high sensitivity, simple configuration, and rapid response time [17–19]. Classical studies have already demonstrated the feasibility of immobilizing AChE on different matrices for pesticide detection, establishing biosensing as a promising alternative to conventional techniques [20].

The performance of such biosensors strongly depends on the material used for enzyme immobilization, which must preserve catalytic activity, ensure operational stability, and promote efficient electron transfer [21–23]. In recent years, significant advances have been achieved using nanomaterials, including carbon nanotubes, graphene and its derivatives, metal oxides, and metallic nanoparticles [20,21]. Among these, gold nanoparticles (AuNPs) have attracted particular attention due to their biocompatibility, chemical stability, unique optical and electronic properties, and the ease of functionalization through Au–S bonding with biomolecules [24–27].

Previous studies have demonstrated that AuNP-based biosensors can reach nanomolar detection limits for carbamates while maintaining good stability and reproducibility [24]. For example, Liu et al. [28], Du et al. [29,30], and Gong [31] reported that incorporating AuNPs into electrode architectures enhances the AChE immobilization efficiency and reduces charge-transfer resistance, thereby improving analytical performance. Nevertheless, challenges remain regarding sustainable synthesis routes and the morphological control of nanoparticles, both of which directly affect the uniformity and reliability of biosensors.

An emerging approach uses self-assembling peptides as reducing and stabilizing agents for the synthesis of metallic nanoparticles [32–35]. The tripeptide cysteine-diphenylalanine (CFF) is particularly promising: its thiol group allows strong interactions with gold surfaces, while the diphenylalanine residue favors self-assembly into stable nanostructures [34]. Recent reports have highlighted that peptide-assisted syntheses not only enable greener routes but also provide superior morphological control, low polydispersity, and enhanced colloidal stability of AuNPs.

In this work, we report the development of an electrochemical biosensor for detecting the pesticide 1-naphthyl N-methylcarbamate (carbaryl), based on the immobilization of acetylcholinesterase onto hydrothermally synthesized gold nanoparticles using the CFF peptide as both a reducing and stabilizing agent. The resulting device demonstrated high sensitivity, nanomolar detection limits, and excellent reproducibility, providing a fast, economical, and sustainable strategy for pesticide monitoring in environmental and agricultural samples. By combining the electrochemical advantages of gold nanoparticles with the self-assembling properties of peptides, this work advances peptide-mediated nanomaterials as versatile platforms for enzymatic biosensing.

2. Experimental

2.1. Materials and Chemicals

Gold(III) chloride trihydrate ($HAuCl_4 \cdot 3H_2O$, Sigma-Aldrich, St. Louis, MO, USA), sodium hydroxide (NaOH, Synth, Diadema, SP, Brazil), sodium phosphate dibasic (Na_2HPO_4, Synth, Diadema, SP, Brazil), sodium phosphate monobasic (NaH_2PO_4, Fisher Scientific, Waltham, MA, USA), sodium iodide (NaI, Synth, Diadema, SP, Brazil), and magnesium sulfate ($MgSO_4$, Synth, Diadema, SP, Brazil) were of analytical grade and used as received. Acetylcholinesterase (AChE) from Electrophorus electricus (electric eel) (Sigma-Aldrich, St. Louis, MO, USA; catalog no. C2888; specific activity ≥ 1,000 U/mg; protein content ≥ 60%), acetylthiocholine chloride (ACTh, Sigma-Aldrich, St. Louis, MO, USA), and 1-naphthyl *N*-methylcarbamate (carbaryl, Sigma-Aldrich, St. Louis, MO, USA) served as biological and analytical reagents.

Peptide synthesis employed Fmoc-Cys(Trt)-OH (Sigma-Aldrich, St. Louis, MO, USA), Fmoc-Phe-OH (Sigma-Aldrich, St. Louis, MO, USA), Wang resin (BACHEM, Bubendorf, Switzerland), 1-hydroxybenzotriazole hydrate (HOBt, Sigma-Aldrich, St. Louis, MO, USA), *N*,*N*′-diisopropylcarbodiimide (DIC, Sigma-Aldrich, St. Louis, MO, USA), *N*-methyl-2-pyrrolidone (NMP, Sigma-Aldrich, St. Louis, MO, USA), *N*,*N*′-dimethylformamide (DMF, Sigma-Aldrich, St. Louis, MO, USA), and 4-methylpiperidine (Sigma-Aldrich, St. Louis, MO, USA). Trifluoroacetic acid (TFA, Sigma-Aldrich, St. Louis, MO, USA) was used for peptide cleavage.

Solvents such as acetonitrile (Honeywell, Charlotte, NC, USA), methanol (Sigma-Aldrich, St. Louis, MO, USA), and dichloromethane (Anidrol, Diadema, SP, Brazil) were of HPLC or analytical grade. Ultrapure water (18.2 MΩ·cm) was obtained from a Milli-Q purification system (Millipore, Burlington, MA, USA).

2.2. Solid-Phase Peptide Synthesis

The CFF was synthesized by Fmoc solid-phase peptide synthesis (SPPS) on a Wang resin pre-functionalized with phenylalanine (Phe-Wang resin) [36]. Equimolar amounts (1.38 mmol) of Fmoc-Cys(Trt)-OH and Fmoc-Phe-OH were sequentially coupled to the resin using *N*,*N*′-diisopropylcarbodiimide (2.75 mmol) and 1-hydroxybenzotriazole (2.75 mmol) in *N*-methyl-2-pyrrolidone (0.1 mmol) for 4 h, with reaction progress monitored by the Kaiser test. Fmoc deprotection of the Nα-terminal was performed with 20% 4-methylpiperidine in dimethylformamide (DMF) for 30 min, followed by washes with methanol and dichloromethane.

Cleavage of the peptide from the resin and simultaneous removal of protecting groups were achieved using a cocktail containing trifluoroacetic acid (TFA), H2O, dithiothreitol (DTT), and triisopropylsilane hydrochloride (TIS·HCl) for 4.5 h at room temperature. The crude peptide was precipitated by centrifugation in cold diethyl ether, washed, and dried under vacuum. A counter-ion exchange step was performed by dissolving the peptide in 0.1 M HCl, then freezing it in liquid nitrogen and lyophilizing to yield the final product.

The CFF peptide used in this study was synthesized according to the previously published Fmoc-SPPS protocol reported by our group [34], where full structural characterization (^{1}H NMR, ^{13}C NMR) and purity assessment (LC/ESI/MS) are described in detail.

2.3. Purification and Characterization

The crude peptide was purified and characterized by high-performance liquid chromatography coupled to mass spectrometry (HPLC-MS, Agilent 6190, Santa Clara, CA, USA). Approximately 1 mg of lyophilized CFF was dissolved in 1 mL of deionized water containing 0.1% TFA, filtered through a 0.22 μm polysulfone membrane, and injected (10 μL) into a C18 reverse-phase column. Elution was carried out in gradient mode with solvent A (water with 0.1% TFA) and solvent B (acetonitrile:water, 90:10 *v*/*v*, with 0.1% TFA).

2.4. Synthesis of Peptide-Coated AuNPs (CFF@AuNPs)

AuNPs stabilized with the tripeptide CFF were synthesized by a hydrothermal method adapted from the classical Turkevich protocol [37], in which the peptide replaced sodium citrate as the reducing and stabilizing agent. Equal volumes (3.2 mL each) of freshly prepared aqueous solutions of $HAuCl_4 \cdot 3H_2O$ (1.16 mM) and CFF (0.40 mM) were mixed, and the pH was adjusted to 7.0 with 0.1 M NaOH. The reaction mixture, containing a Teflon-coated magnetic stir bar, was heated in a water bath at 65 ± 2 °C and stirred for 90 min to reduce Au^{3+} ions and stabilize the nanoparticles.

The formation of AuNPs was evidenced by a characteristic color change in the solution and confirmed by UV-Vis spectroscopy, which showed a surface plasmon resonance band centered at 525 nm, indicative of spherical AuNPs. Further morphological analysis by SEM and TEM corroborated the uniformity and spherical shape of the resulting nanostructures.

2.5. Preparation of Modified Carbon Electrodes and Electrochemical Setup

Commercial screen-printed carbon electrodes (SPEs, DropSens, Oviedo, Spain) were used as the electrochemical platform. Each SPE contains a carbon working electrode (4 mm diameter), a carbon counter electrode, and an Ag/AgCl pseudo-reference electrode. For surface modification, 15 μL of each dispersion was drop-cast onto the working electrode area: (i) AuNPs stabilized with the CFF peptide (CFF@AuNPs), (ii) the CFF peptide alone, or (iii) acetylcholinesterase (AChE) immobilized on CFF@AuNPs. The electrodes were dried at room temperature before use.

Electrochemical measurements—including cyclic voltammetry (CV), electrochemical impedance spectroscopy (EIS), chronoamperometry, and square-wave voltammetry (SWV)—were carried out using a Metrohm PGSTAT302N potentiostat equipped with a DropSens cell cable and dummy cell for electrode connection. All measurements were performed under unstirred conditions at room temperature (22–25 °C).

For electrode characterization, the reversible $[Fe(CN)_6]^{3-/4-}$ redox couple (5.0 mM in 100 mM sodium phosphate buffer, pH 7.0) was used as an outer-sphere probe. This pH was selected because neutral conditions ensure optimal electrochemical stability at the electrode–solution interface, minimize capacitive background currents, and preserve the native protonation states of both the CFF peptide and the AuNP surface, leading to highly reproducible voltammetric and impedance responses.

Cyclic voltammograms were acquired over the potential range from −0.2 to +0.6 V (vs. Ag/AgCl) at scan rates of 10–200 mV s^{-1}. The heterogeneous electron-transfer rate constant (k_0) was determined using the Laviron method, which is appropriate for quasi-reversible systems on surface-modified electrodes [38]. For each modified

surface, the anodic and cathodic peak potentials (E_{pa} and E_{pc}) were plotted as a function of log *v*. From the linear regions of these Laviron plots, the charge-transfer coefficient (α) and k_0 were extracted using:

$$E_p = E^0 + \left(\frac{2.303\,RT}{\alpha nF}\right)\log\left(\frac{RTk_0}{\alpha nF}\right) + \left(\frac{2.303\,RT}{\alpha nF}\right)\log v \quad (1)$$

where *n* is the number of electrons transferred and *F*, *R*, and *T* have their conventional meanings.

Electrochemical impedance spectroscopy was recorded in the frequency range from 100 kHz to 0.1 Hz using a 10 mV AC perturbation at the formal potential of the redox probe. The impedance data were fitted using a Randles-type equivalent circuit to extract charge-transfer resistance (R_{ct}) values, which support the interpretation of electron-transfer kinetics.

For pesticide detection and inhibition assays, chronoamperometric measurements were performed using the CFF@AuNPs–AChE-modified electrodes in 100 mM sodium phosphate buffer at pH 8.0 containing acetylthiocholine (ATCh) as the enzymatic substrate. A constant potential was applied (as specified in the Results section), and the resulting current was monitored as a function of time. Under these conditions, the measured faradaic current arises from the electrochemical oxidation of thiocholine produced by the AChE-catalyzed hydrolysis of ATCh. It is therefore directly proportional to the enzymatic activity at the electrode surface.

For inhibition experiments, the electrode was exposed to increasing concentrations of carbaryl, and the steady-state current recorded after inhibitor addition (*I*) was compared to the current measured in the absence of inhibitor (I_0). The inhibition efficiency was calculated according to:

$$Inhibition\ efficiency\ (\%) = \frac{I_0 - I}{I_0} \times 10 \quad (2)$$

where I_0 represents the chronoamperometric current in the absence of carbaryl, and *I* corresponds to the current measured after incubation with a given inhibitor concentration. All inhibition measurements were conducted at pH 8.0, which corresponds to the optimal catalytic range of acetylcholinesterase from Electrophorus electricus, according to the manufacturer's specifications (Sigma-Aldrich, C2888) and supported by literature reports indicating maximal AChE activity near physiological pH [39].

The limit of detection (LOD) was calculated using the 3σ criterion, defined as three times the standard deviation of the blank signal divided by the slope of the calibration curve (LOD = 3 σ_{blank}/S). The blank signal was obtained from repeated chronoamperometric measurements performed in the absence of carbaryl under identical experimental conditions, and the slope was extracted from the linear region of the calibration plot.

2.6. Physicochemical and Structural Characterization

2.6.1. UV-Vis Spectroscopy

UV-Vis spectra were acquired using a Varian Cary 50 spectrometer and quartz cells with a 1.0 cm path length. The spectral resolution for wavelength scanning was 1.0 nm.

2.6.2. Dynamic Light Scattering (DLS)

DLS measurements were performed using an ALV/CGS-3 platform-based goniometer system (ALV GmbH) equipped with a polarized HeNe laser (22 mW at 633 nm), an ALV 7004 digital correlator, and a pair of APD-based single-photon detectors. Samples were loaded into 10 mm diameter glass cuvettes and maintained at 25 °C. The data were collected using the ALV Correlator Control software with a 60 s counting time. The autocorrelation functions were acquired at 25 °C in triplicate at 90° scattering angle (θ), then averaged before analysis using the CONTIN algorithm incorporated into the ALV correlator control software. The resulting relaxation time distributions were further converted into hydrodynamic radius (R_H) distributions by using the Stokes-Einstein equation:

$$R_H = \frac{k_B T q^2}{6\pi\eta}\tau \quad (3)$$

where k_B is the Boltzmann constant, *T* is the absolute temperature, *q* is the scattering vector, η is the solvent viscosity, and τ is the mean relaxation time. The autocorrelation functions ($g_1(t)$) were also analyzed using the Cumulant method (second-order cumulant) [40].

$$ln\, g_1(t) = ln\, C - \Gamma t + \frac{\mu_2}{2}t^2 \quad (4)$$

where *C* is the amplitude of the autocorrelation function, Γ is the relaxation frequency (τ^{-1}), and the parameter μ_2 is known as the second-order cumulant. This approach enabled the determination of polydispersity indices (PDI = μ_2/Γ^2) for monomodal size distributions.

2.6.3. Electrophoretic Light Scattering (ELS)

The electrophoretic mobility of the prepared particles was measured using a Malvern Zetasizer Nano-ZS apparatus (model ZEN3600, Malvern Instruments Ltd., Malvern, UK) to evaluate their surface charge. The measurements were performed in folded capillary cuvettes (DTS1070, Malvern Instruments Ltd., Malvern, UK) containing 800 µL of the samples at a concentration of 0.025 mg·mL^{-1}. The ζ-potential (zeta potential) values were derived from electrophoretic mobility (U_E) data using the Henry equation and assuming the Smoluchowski approximation for aqueous samples ($f(\kappa a)$ = 1.5) [41,42].

$$U_E = \frac{2\varepsilon\zeta}{3\eta} f(\kappa a) \quad (5)$$

where ε is the dielectric constant of the medium and η its viscosity.

2.6.4. Transmission Electron Microscopy

High-resolution transmission electron microscopy was performed using a Talos F200X G2 microscope (Thermo Fisher Scientific, Hillsboro, OR, USA), equipped with a cold-field emission gun (FEG-X) and a scanning transmission electron microscopy (STEM) module, operating at 200 keV. For sample preparation, 4 µL of the CFF@AuNPs dispersion was drop-cast onto perforated copper grids (400 mesh) coated with a thin carbon support film. The grids were dried under vacuum in a desiccator for 24 h before imaging.

2.6.5. Scanning Electron Microscopy (SEM)

SEM was performed using a field-emission scanning electron microscope (FESEM; JSM-6701F, JEOL Ltd., Tokyo, Japan) operating under ultra-high vacuum. Samples were prepared by drop-casting 15 µL of the CFF@AuNPs dispersion onto the working area of commercial carbon-based screen-printed electrodes. After drying, the electrodes were mounted on copper stubs using conductive carbon tape. Imaging was performed at 5 kV to visualize the metallic nanostructures and peptide assemblies associated with the gold nanoparticles.

2.6.6. Atomic Force Microscopy (AFM) Measurements

Thin films of the CFF peptide and CFF@AuNPs were prepared by drop-casting the corresponding dispersions onto freshly cleaved mica substrates and allowed to dry at room temperature. Atomic force microscopy (AFM) measurements were performed using a MultiMode VIII AFM (Bruker, Santa Barbara, CA, USA) operating in tapping mode at the Brazilian Nanotechnology National Laboratory (LNNano, Campinas, Brazil). Imaging was carried out using a silicon cantilever with a nominal force constant of 2.8 N m^{-1} and a nominal resonance frequency of ~75 kHz.

AFM images were acquired at 512 × 512 pixels, covering scan areas ranging from 0.1 to 5.0 µm². Topography and phase images were recorded to assess surface morphology and nanoscale organization. Image processing and analysis were performed using the Gwyddion software package (version 2.63).

2.6.7. X-Ray Photoelectron Spectroscopy (XPS)

XPS analyses were carried out on a Thermo Scientific K-Alpha spectrometer (Thermo Fisher Scientific, East Grinstead, UK), using a monochromatic Al Kα X-ray source (1486.6 eV). The surfaces of commercial SPEs, either unmodified or modified with AuNPs stabilized by the CFF peptide, were analyzed. For each condition, samples were prepared in triplicate to ensure reproducibility. Survey and high-resolution spectra were collected for the elements C 1s, N 1s, O 1s, S 2p, and Au 4f to confirm the presence of Au–S bonds and evaluate the chemical composition of the electrode surfaces. The binding energy scale was calibrated using the hydrocarbon C 1s peak at 285.0 eV. Data acquisition and fitting were performed using Thermo Avantage software (version 5.921), which applied Voigt functions for peak deconvolution and Scofield sensitivity factors for quantitative analysis.

3. Results and Discussion

3.1. Synthesis and Characterization of Peptide-Coated AuNPs

The CFF compound was successfully synthesized using Fmoc-based solid-phase peptide synthesis on Wang resin [36], an efficient solid support for the sequential addition of phenylalanine and cysteine residues [34]. The protection of functional groups during synthetic steps was crucial to prevent side reactions. At the same time, deprotection with 4-methylpiperidine, followed by thorough washing, ensured selective removal of the Fmoc protecting group without compromising peptide integrity. The overall synthetic pathway is depicted in Figure S1.

HPLC-MS analyses confirmed the identity and purity of the synthesized CFF peptide (Figure S2). The chromatogram showed a sharp, well-defined peak at approximately 23 min, consistent with a single major product. Electrospray ionization mass spectrometry further validated the molecular structure, revealing a dominant signal at m/z 416.2, corresponding to the $[M + H]^+$ ion of the expected tripeptide, with a relative abundance of 99.98%. These results confirmed the chemical structure and high purity of the synthesized CFF peptide, supporting its suitability as a reducing and stabilizing agent for the subsequent preparation of peptide-coated AuNPs.

Following the synthesis of the CFF peptide, gold nanoparticles were prepared using the tripeptide as both reducing and stabilizing agent. Optimal colloidal stability was achieved when equimolar volumes of aqueous $HAuCl_4$ (1.16 mM) and CFF (0.40 mM) solutions were mixed, corresponding to a peptide-to-gold molar ratio of approximately 1:3 at pH 7. Under these conditions, the peptide not only mediated the reduction of Au^{3+} ions to metallic gold but also acted as a capping ligand, yielding a stable colloidal dispersion with a well-defined plasmonic response.

The optical properties of the CFF@AuNPs colloid were investigated by UV-Vis spectroscopy (Figure 1a). The spectrum displayed a well-defined surface plasmon resonance band centered at ~525 nm, a signature feature of spherical gold nanoparticles. The narrowness of the band indicated a relatively homogeneous particle size distribution and efficient stabilization by the peptide layer. The absence of additional absorption features in the near-UV region also confirmed that the peptide did not interfere spectrally with the plasmonic response of the nanoparticles.

DLS further evaluated colloidal stability and hydrodynamic size distribution. The autocorrelation function (Figure 1b) displayed a smooth exponential decay, characteristic of a stable colloidal system. The size distribution profile (Figure 1c) showed a monomodal population with an average hydrodynamic radius of 16.25 nm and a low polydispersity index (PDI), indicating the homogeneity of the dispersion. In addition, the ζ-potential value of –29.4 ± 0.1 mV corroborated the high colloidal stability of the CFF@AuNPs system, consistent with literature values for well-stabilized gold nanoparticles [43].

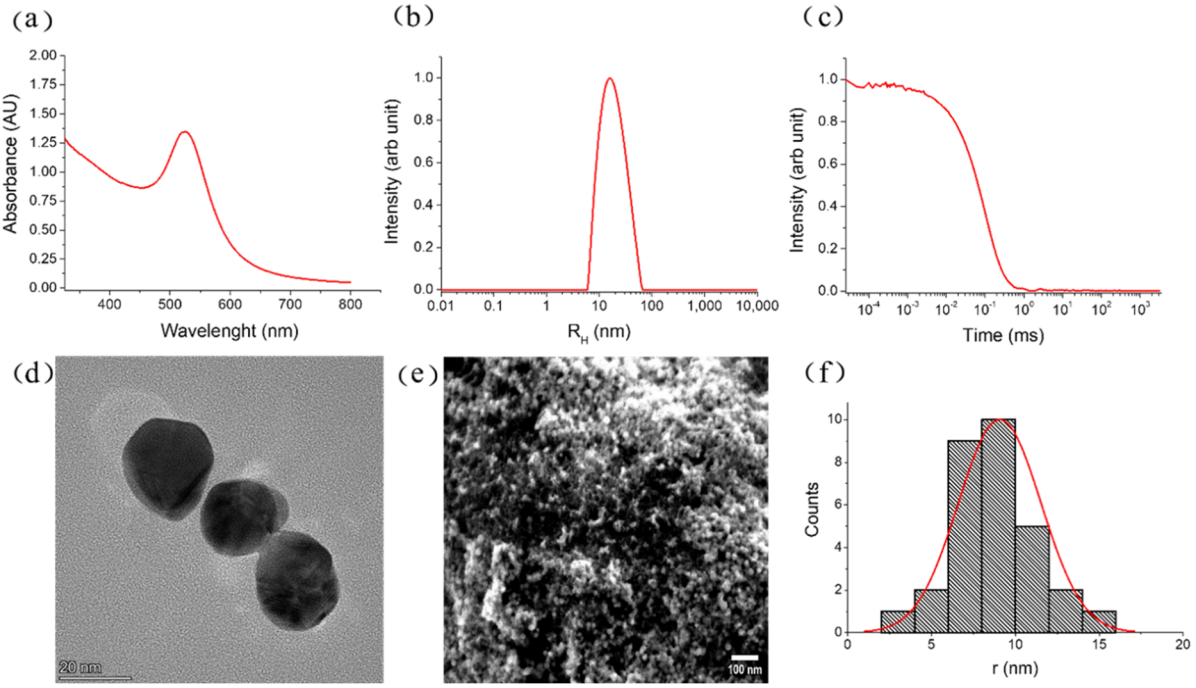

Figure 1. (**a**) UV-Vis spectrum of CFF@AuNPs; (**b**) DLS correlation curve from; (**c**) frequency distribution of hydrodynamic radius; (**d**) TEM micrograph; (**e**) SEM micrograph; and (**f**) corresponding TEM histogram size distribution.

TEM provided direct evidence of the morphology and size of the CFF@AuNPs (Figure 1d). The nanoparticles exhibited predominantly spherical shapes with well-defined contours and an average radius of 8.4 ± 2.8 nm, as determined from statistical analysis of multiple images. The relatively narrow distribution confirmed the efficiency of the peptide in mediating the nucleation and growth of gold nanostructures with controlled dimensions.

In contrast to TEM, SEM imaging (Figure 1e) does not resolve individual CFF@AuNPs, whose 10–20 nm dimensions fall below the practical resolution limit for conventional SEM on carbon-based electrodes. Instead, SEM captures the mesoscale surface morphology arising from the supramolecular organization of the

peptide-nanoparticle assemblies after deposition. The heterogeneous granular domains observed in the micrographs, therefore, reflect peptide-induced aggregation and film formation rather than the primary particle size.

This interpretation is supported by AFM measurements included in the Supplementary Information (Figure S3), which reveal nanoscale aggregates, roughness domains, and surface features that closely match those observed in SEM. AFM thus provides independent topographical evidence for the hierarchical supramolecular organization of the CFF-stabilized AuNP film upon deposition on the electrode surface.

It is worth noting that the dimensions obtained from electron microscopy were consistently smaller than the hydrodynamic radius measured by DLS (16.25 nm, PDI < 0.2). This discrepancy is well documented in the literature and is attributed to the fact that DLS accounts not only for the metallic core but also for the solvation layer and peptide corona surrounding nanoparticles in solution. In contrast, TEM and SEM probe only the dry metallic core under high vacuum. Together, these complementary techniques confirm the successful synthesis of monodisperse, colloidally stable AuNPs functionalized with CFF.

XPS was employed to investigate the chemical environment of the peptide-coated gold nanoparticles deposited on the surface of carbon-based screen-printed electrodes. The survey spectra confirmed the presence of carbon, nitrogen, oxygen, sulfur, and gold, consistent with the expected composition of the CFF-modified nanostructures (Figure 2a–c).

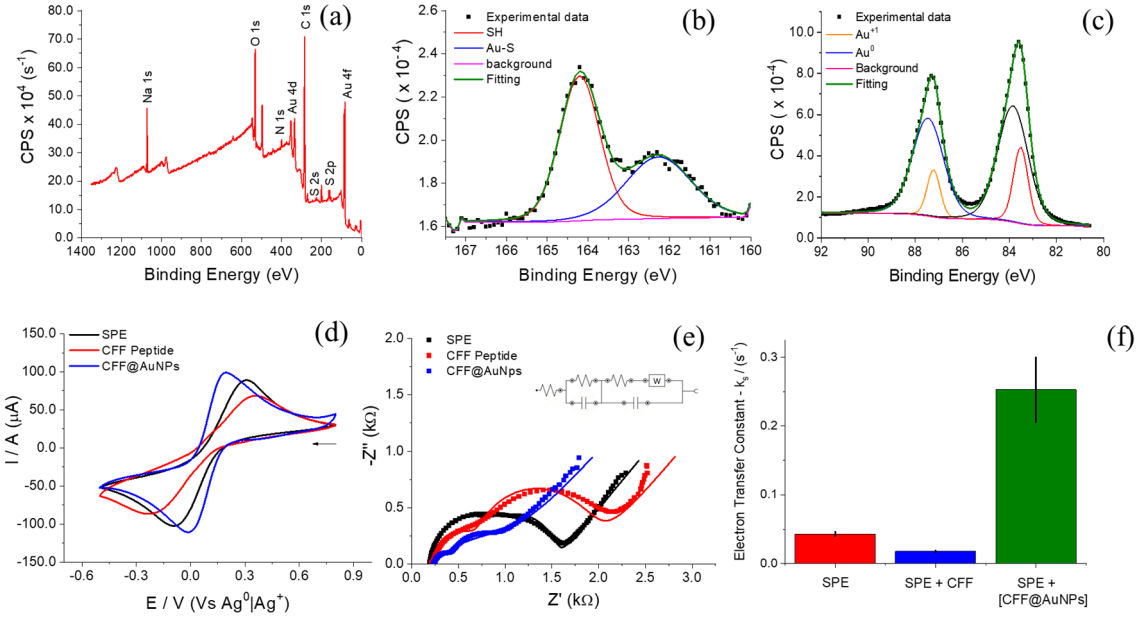

Figure 2. High-resolution XPS spectra of the (**a**) overall survey of the carbon-based screen-printed electrode (SPE) modified with gold nanoparticles synthesized using the CFF peptide, and the corresponding (**b**) S 2p and (**c**) Au 4f regions. Comparative electrochemical characterization by (**d**) cyclic voltammetry and (**e**) electrochemical impedance spectroscopy (EIS) for the bare SPE (black dots), crude CFF peptide (red dots), and CFF@AuNPs-modified electrode (blue dots), recorded in the presence of the outer-sphere redox probe $[Fe(CN)_6]^{3-/4-}$ (5.0 mM in 100 mM sodium phosphate buffer, pH 7.0). The electrochemical responses reflect changes at the electrode surface induced by the deposited peptide and peptide-AuNP films. The respective solid lines represent the data fitting using the modified Newman equivalent circuit, in which the double-layer capacitance was replaced by a constant phase element (CPE). (**f**) Bar graph showing the enhancement of the heterogeneous electron-transfer rate constant (k_0) after modification with CFF@AuNPs.

The high-resolution sulfur spectrum (Figure 2b) revealed two distinct S 2p doublets, assigned to thiolate species bound to gold (Au–S) and free thiol groups (–SH). The component at ~162.3 eV is characteristic of Au–S bonding, whereas the signal centered at ~164.2 eV corresponds to unbound thiols. This result indicates that a fraction of the cysteine residues of the CFF peptide is covalently anchored to the Au nanoparticle surface, contributing to colloidal stabilization, while another fraction remains non-coordinated. Such coexistence is consistent with a mixed binding scenario, in which peptide molecules are stabilized on the nanoparticle surface through both covalent Au–S interactions and noncovalent interactions associated with peptide self-assembly and supramolecular organization [34].

The high-resolution spectrum of gold (Figure 2c) showed four characteristic peaks, grouped into two pairs. Peaks at 83.88 eV and 87.46 eV were attributed to metallic gold (Au^0), confirming the successful reduction of the precursor salt. Additional peaks at 83.51 eV and 85.26 eV indicated the presence of Au^{+1} species, directly associated with the covalent Au–S interaction between the nanoparticles and the thiol groups of the peptide. The coexistence of Au^0 and Au^{+1} states is consistent with previous reports describing the peptide-mediated stabilization of gold nanostructures, where partial oxidation occurs at the peptide-gold interface.

Together, these XPS analyses provided unambiguous evidence of the successful chemical functionalization of gold nanoparticles with the CFF peptide, confirming the role of cysteine residues in mediating both reduction and surface stabilization. These findings corroborate the morphological and colloidal characterization, further establishing that the synthetic strategy yielded structurally and chemically stable CFF@AuNPs.

Electrochemical characterization of the peptide-coated gold nanoparticles was carried out by CV and EIS using carbon-based screen-printed electrodes modified with CFF@AuNPs. The CV profiles (Figure 2d) showed a significant increase in both anodic and cathodic peak currents relative to bare electrodes, confirming the successful surface modification and the improved electron-transfer properties provided by the nanostructured layer. Specifically, the anodic and cathodic peak currents increased by a factor of 2 relative to the bare SPE, and the peak-to-peak separation (ΔE_p) decreased to ~100 mV, indicating faster electron-transfer kinetics and behavior closer to reversibility. This enhancement can be attributed to the high surface area of the nanoparticles and the conductive properties of the gold core, which facilitated charge transfer at the electrode–electrolyte interface [44].

The cyclic voltammograms recorded at multiple scan rates (10–200 mV s^{-1}), which were used to extract the peak-potential shifts required for the kinetic evaluation, are provided in the Supplementary Information (Figure S4).

The heterogeneous electron-transfer rate constant (k_0) obtained from Laviron analysis revealed a substantial improvement upon surface modification: the bare carbon electrode displayed a k_0 value of 0.04 s^{-1}, whereas the CFF@AuNPs-modified electrode reached 0.25 s^{-1} (Figure 2f). This pronounced enhancement is fully consistent with the CV and EIS results and reflects the increased electroactive surface area and improved interfacial conductivity provided by the peptide-stabilized gold nanoparticles.

EIS measurements (Figure 2e), fitted using a modified Newman equivalent circuit in which the double-layer capacitance was replaced by a constant phase element (CPE), further corroborated these findings [45]. The Nyquist plots of the CFF@AuNPs-modified electrodes exhibited a pronounced decrease in the charge-transfer resistance (R_{ct}) compared to the unmodified electrodes, as evidenced by the smaller semicircle diameter in the high-frequency region. Specifically, the R_{ct} decreased from approximately 1.6 kΩ for the bare carbon electrode to about 0.45 kΩ after modification with CFF@AuNPs, confirming the peptide's ability to promote a uniform distribution of gold nanoparticles and enhance interfacial charge transfer. This reduction in interfacial resistance reflects not only faster electron-transfer kinetics but also the increased electroactive surface area and improved conductivity provided by the nanostructured coating.

3.2. Immobilization of AChE and Detection of Carbaryl

The immobilization of AChE onto CFF@AuNPs-modified electrodes was achieved by drop-casting equal volumes of the colloidal CFF@AuNPs dispersion and the enzyme stock solution. The optimized condition corresponded to a final enzyme concentration of 33.4 U·mL^{-1}, which provided a stable current response with minimal deviation at equilibrium (600–1200 s), outperforming higher enzyme loadings typically reported in the literature (e.g., 80–127 U·mL^{-1}) [46,47].

Cyclic voltammetry measurements (Figure 3a) confirmed the enzymatic hydrolysis of acetylthiocholine (ATCh) by AChE immobilized on CFF@AuNPs, producing thiocholine as the electroactive species [48]. A distinct oxidation peak appeared between 0.6 and 0.8 V, which was absent in the control without enzyme, demonstrating that the CFF peptide alone does not exhibit catalytic or mimetic activity.

Chronoamperometric studies (Figure 3b) further validated these findings, revealing an increase in oxidation current with increasing ATCh concentration. Electrodes prepared with 33.4 U·mL^{-1} AChE exhibited the most intense and stable current response, confirming this as the optimal enzyme loading. These results highlight the synergy between the CFF@AuNPs nanostructure and AChE, in which the peptide provides a biocompatible interface and strong anchoring through Au–S interactions, thereby preserving enzymatic activity.

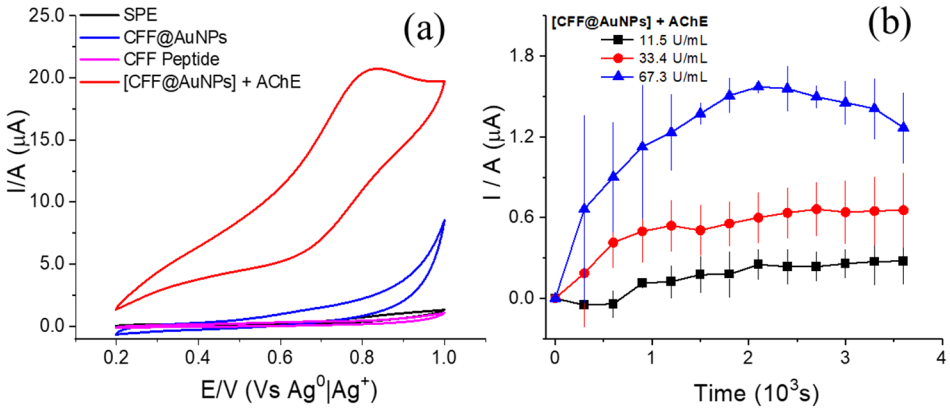

Figure 3. (**a**) Cyclic voltammetry comparison of the bare SPE (black line), CFF@AuNPs-modified electrode (blue line), crude CFF peptide (pink line), and CFF@AuNPs–AChE-modified electrode (red line) recorded in the presence of acetylthiocholine (ATCh), illustrating the electrochemical response associated with enzymatic hydrolysis and subsequent oxidation of thiocholine at the electrode surface. (**b**) Chronoamperometric response of the CFF@AuNPs–AChE-modified electrode toward increasing concentrations of ATCh, where the steady-state current reflects the catalytic activity of the immobilized acetylcholinesterase, and was used for the quantitative evaluation of enzymatic activity and inhibition efficiency.

SWV experiments (Figure 4a) confirmed the enzymatic activity of AChE immobilized on the CFF@AuNPs-modified electrode, showing a well-defined oxidation peak at 0.75 ± 0.02 V, consistent with the electrochemical oxidation of thiocholine as previously reported [49–52].

Calibration experiments with carbaryl in the range of 1–6 nM (Figure 4b) yielded a linear relationship between the inhibition percentage and the logarithm of carbamate concentration, described by the regression equation:

$$\% \text{ Inhibition} = 0.4302 \times \log[C] + 4.3453 \ (R^2 = 0.99)$$

From this calibration, the biosensor exhibited a limit of detection (LOD) of 0.94 nM, which is notably lower than most reported values for AChE-based biosensors using gold or carbon nanostructures (Table 1). This improvement highlights the high sensitivity achieved with the peptide-stabilized AuNPs interface. Reproducibility tests yielded relative standard deviations of less than 5% ($n = 3$), confirming the robustness of the fabrication procedure.

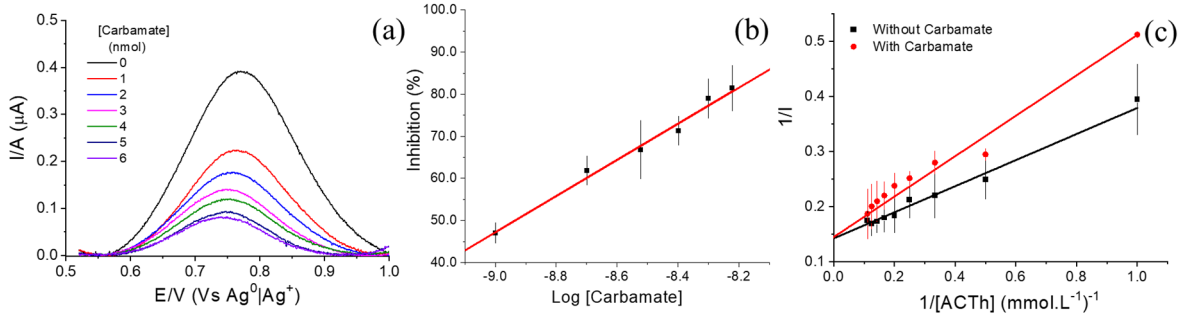

Figure 4. (**a**) Square wave voltammograms of the AChE/CFF@AuNPs-modified SPE obtained for increasing concentrations of 1-naphthyl *N*-methylcarbamate. (**b**) Calibration curve showing the percentage of inhibition as a function of the logarithm of carbamate concentration. (**c**) Lineweaver–Burk plot for the AChE/CFF@AuNPs-modified electrode in the absence and presence of the pesticide, confirming the mixed inhibition behavior.

Enzyme kinetics were further evaluated using the Michaelis–Menten model (Figure 4c), obtained from chronoamperometry at 0.75 V with increasing ATCh concentrations (1–9 mM) [52]. The biosensor displayed a Michaelis–Menten constant (K_m) of 1.66 mM in the absence of inhibitor, confirming the high affinity of AChE immobilized on CFF@AuNPs for its substrate. Upon exposure to carbaryl (3.5 nM, 2 min), the apparent K_m increased to 2.52 mM, while the maximum velocity (V_{max}) remained unchanged, indicating a competitive inhibition mechanism. This behavior aligns with the classical inhibition pattern of AChE by carbamate pesticides. The inhibition constant (k_i) for carbaryl was estimated to be 1.14×10^7 M^{-1} min^{-1}, consistent with values reported for AChE-based biosensors [53].

These results highlight the potential of peptide-mediated nanostructures as efficient immobilization platforms for enzymatic biosensors, enabling highly sensitive and selective detection of pesticides at environmentally relevant concentrations.

Table 1. Comparison of analytical performance reported for AChE-based biosensors employing different electrode architectures, enzyme immobilization strategies, and detection techniques, including the present study (compiled from literature reports and this work).

Technique	Target Inhibitor(s)	Electrode Architecture	Immobilization strategy	LOD	Linear range	Reference
Colorimetric	Methomyl, Profenofos	CS/DTNB	Covalent crosslinking (glutaraldehyde)	6.16×10^{-4} mM	0.27 mM	[54]
Potentiometric	Malathion, Parathion-methyl, Methamidophos	CS/pH electrode	Ionic interaction	0.6–600 mM	0.1–100 mM	[55]
Amperometric (CV)	Malathion	AChE-CS-AuNPs/Au	Ionic interaction	0.1 nM	0.1–20 ng/mL	[30]
Amperometric (CV)	Phoxim	AChE@CCS/AgNC/ rGO/GCE	Covalent crosslinking (carboxylic chitosan)	0.081 nM	0.2–250 nM	[56]
Amperometric (CV)	Methyl parathion	AChE-$CaCO_3$ NPs-CS/GCE	Diffusion-controlled	1 ng/mL	0.005–0.2 µg/mL	[57]
Amperometric (DPV)	Dichlorvos	AChE/CS@TiO_2-CS/ rGO/GCE	Electrostatic interaction	29 nM	0.036–22.6 µM	[58]
Amperometric (DPV)	Malathion	AChE-CS/ Pd-Cu NWs/GCE	Physical adsorption	1.5 ppt	5–1000 ppt	[59]
Amperometric (DPV)	Malathion, Carbaryl	CS/AChE/ PB-CS/ERGO/ AuNPs-β-CD/GCE	Physical adsorption	4.14 pg/mL| 1.15 pg/mL	$7.98–2.0 \times 10^3$ pg/mL| $4.3–1.0 \times 10^3$ pg/mL	[60]
Amperometric (LSV)	Captan, Carbosulfan, TCDD, and PCP	Pt/ZnO/AChE/CS	Ionic interaction	1–50 nM	0.05–30 µM	[61]
Amperometric (CV)	Chlorpyrifos	Nafion/AChE/MWNTs-SnO_2-CS/Au	Physical adsorption	100 µg/L	$0.05–1 \times 10^5$	[62]
Amperometric (CV)	Triazophos	AChE-MC/GCE	Covalent crosslinking (glutaraldehyde)	0.01 µM	0.03–7.8 µM	[63]
Amperometric (CV)	Monocrotophos	AChE-CdTe-GNPs-CM/GCE	Covalent attachment	0.3 ng/mL	1–1000 ng/mL	[64]
Amperometric (CV)	Dichlorvos, Omethoate, Trichlorfon, Phoxim	AChE-PB/GCE	Covalent crosslinking (glutaraldehyde)	2.5–15 ng/L	10–10,000 ng/L	[65]
Amperometric (CV)	Dichlorvos	$(MWCNTs/ALB)_6$/ GCE	Ionic interaction	0.68 µg/L (±0.076)	0.25–1.75 µM	[66]
Amperometric (SEV)	Dichlorvos	$(CS/ALB)_5$/GCE	Ionic interaction	0.86 µg/L (±0.098)	0.25–1.50 µM	[67]
Amperometric (CV)	Dichlorvos	AChE-AN-MWNTs/ GCE	Physical adsorption	10 ng/L	50 ng/L–5 mg/L	[68]
Amperometric (CV)	Methomyl	(AChE/CS)/ (MWNTs/CS)/GCE	Ionic interaction	10^{-11} g/L	$10^{-10}–10^{-3}$ g/L	[69]
Amperometric (CV & Chronoamperometry)	Methyl parathion	AChE/F-ZnSe/ GR-CS/GCE	Physical adsorption	0.2 nM	0.5 nM–0.5 µM	[70]
Amperometric (CV)	Malathion	AChE-MWCNTs-Au-CS/GCE	Physical adsorption	0.6 ng/mL	1–1000 ng/mL	[71]
Amperometric (DPV)	Malathion, Chlorpyrifos, Monocrotophos, Carbofuran	AChE/CS-PB-MWNTs-HGNs/Au	Physical adsorption	0.05 nM	0.05–80 nM	[72]
Amperometric (FIA)	Sulfotep	AChE/CMC/GCE	Covalent attachment (glutaraldehyde)	1.0 nM	1.0–500 µM	[73]
Amperometric	Pirimiphos-methyl	AChE/CS-PVANFM/SPE	Covalent crosslinking (glutaraldehyde)	0.2 nM	NR	[74]
Amperometric (CV & Chronoamperometry)	Paraoxon	AChE/CS/CB-SPE	Physical adsorption	0.05 µg/L	0.1–0.5 µg/L	[75]
Amperometric (SEV)	Malathion, Monocrotophos	AChE-CS/GNPs/Au	Physical adsorption	0.01 µg/mL 0.001 µg/ml	0.001–0.1 µg/mL 2–20 µg/ml	[76]
Amperometric (CV)	Phoxim, Malathion, Dimethoate	GC/ZrO_2/CS/AChE	Physical adsorption	1.3×10^{-6} M (Phoxim); 5.0×10^{-9} M (Malathion); 1.7×10^{-6} M (Dimethoate)	Phoxim: $6.6 \times 10^{-6}–4.4 \times 10^{-4}$ M; Malathion: $1.0 \times 10^{-8}–5.9 \times 10^{-7}$ M; Dimethoate: NR	[77]
Amperometric (CV & Chronoamperometry)	Chlorpyrifos, Malathion, Carbofuran, Isoprocarb	AChE/CPBA/AuNPs/ rGO-CS/GCE	Covalent bonding (esterification)	1.1 ppb; 0.5 ppb; 0.05 ppb; 0.5 ppb	0.5–10 ppb; 0.5–10 ppb; 0.1–10 ppb; 2–10 ppb	[78]
Amperometric (SWV)	Carbaryl	AChE/CFF@AuNPs/ SPE-C	Physical Adsorption	0.94 nM	2–6 nM	This Work

4. Conclusions

In this work, we developed an electrochemical biosensor for detecting carbamate pesticides, based on acetylcholinesterase immobilized on gold nanoparticles synthesized using the CFF peptide as both a reducing and stabilizing agent. The peptide-mediated synthesis produced spherical AuNPs with a controlled hydrodynamic radius (~16 nm), low polydispersity, and high colloidal stability, as confirmed by several techniques, including XPS analysis. Electrochemical studies revealed that the nanostructured interface substantially enhanced electron transfer, as evidenced by lower charge-transfer resistance and a higher heterogeneous electron-transfer rate constant compared to the bare electrode.

The biosensor exhibited excellent analytical performance for carbaryl detection, with a Michaelis–Menten constant of 1.66 mM (increasing to 2.52 mM after exposure to the pesticide), an inhibition constant of 1.14×10^7 $M^{-1} \cdot min^{-1}$, and a highly linear calibration curve. The device achieved a detection limit of 0.94 nM, outperforming most reported AChE-based biosensors. Moreover, the optimized enzyme loading (33.4 $U \cdot mL^{-1}$) ensured stable, reproducible responses (RSD < 5%) while maintaining a low-cost, sustainable fabrication strategy.

Overall, these findings demonstrate that peptide-mediated gold nanostructures constitute a versatile and efficient platform for enzyme immobilization and biosensing. The combination of the CFF peptide's self-assembling properties and the electronic conductivity of gold nanoparticles provided a sensitive and reproducible interface for AChE immobilization. This approach contributes to a fundamental understanding of peptide-nanoparticle interactions and supports the design of greener, more stable electrochemical biosensing architectures.

Supplementary Materials

The additional data and information can be downloaded at: https://media.sciltp.com/articles/others/26011614224587 19/BB-25100137-Supplementary-Materials.pdf. Supporting Information includes the Fmoc solid-phase synthesis scheme and HPLC-MS characterization of the CFF peptide, AFM and XPS surface analyses, and complementary electrochemical data. The Supplementary Material also presents cyclic voltammograms recorded at multiple scan rates, Laviron plots, and a summary table reporting the charge-transfer coefficient (α) and heterogeneous electron-transfer rate constant (k_0) for bare and CFF@AuNPs-modified electrodes.

Author Contributions

M.R.deA.S.: conceptualization, methodology, investigation, data curation, writing—original draft preparation. B.B.G.: methodology, investigation, data curation, writing—review and editing. A.C.H.deC.-K.: investigation, validation, data curation. A.M.A.: investigation, resources, validation. W.A.A.: conceptualization, supervision, project administration, funding acquisition, writing—review, and editing. All authors have read and agreed to the published version of the manuscript.

Funding

This research was funded by the São Paulo Research Foundation (FAPESP), Brazil (Process Nos. 2024/00989-7 and 2022/14753-0); the National Council for Scientific and Technological Development (CNPq, Grant No. 305574/2023-0); and the National Institute of Science and Technology in Bioanalytics—Lauro Kubota (INCTBio-LK) (CNPq Grant No. 408338/2024-5; FAPESP Process No. 2025/26623-1). This study was also partially funded by the Coordination for the Improvement of Higher Education Personnel—Brazil (CAPES, Finance Code 001).

Institutional Review Board Statement

Not applicable.

Informed Consent Statement

Not applicable.

Acknowledgements

The authors are grateful to the Multiuser Central Facilities at UFABC for infrastructure and technical support.

Conflicts of Interest

The authors declare no conflict of interest.

Use of AI and AI-Assisted Technologies

No AI tools were utilized for this paper.

References

1. Xiumei, H.; Vimal, K, B.; Vanloon, W.G.; et al. Degradation of the Pesticide Fenitrothion as Mediated by Cationic Surfactants and α-Nucleophilic Reagents. *Langmuir* **2006**, *22*, 9009–9017.
2. Scognamiglio, V.; Rea, G.; Arduini, F.; et al. *Biosensors for Sustainable Food-New Opportunities and Technical Challenges*; Elsevier: Amsterdam, The Netherlands, 2016; Volume 74, pp. 3–342.
3. Gerbelli, B.B.; Sodre, P.T.; Filho, P.L.O.; et al. Enhancing pesticide detection: The role of serine in lipopeptide nanostructures and their self-assembly dynamics. *J. Colloid Interface Sci.* **2025**, *690*, 137271.
4. Gerbelli, B.B.; Filho, P.L.O.; Cortez, B.; et al. Interaction between glyphosate pesticide and amphiphilic peptides for colorimetric analysis. *Nanoscale Adv.* **2022**, *4*, 3592–3599.
5. Tankiewicz, M.; Fenik, J.; Biziuk, M. Determination of organophosphorus and organonitrogen pesticides in water samples. *TrAC Trends Anal. Chem.* **2010**, *29*, 1050–1063.
6. Oliveira, T.M.B.F.; Ribeiro, F.W.P.; Souza, C. P.; et al. Current overview and perspectives on carbon-based (bio)sensors for carbamate pesticides electroanalysis. *Trends Anal. Chem.* **2020**, *124*, 115779.
7. Kim, K.; Tsay, O.G.; Atwood, D.A.; et al. Destruction and detection of chemical warfare agents. *Chem. Rev.* **2011**, *111*, 5345–5403.
8. Aragay, G.; Pino, F.; Merkoçi, A. Nanomaterials for sensing and destroying pesticides. *Chem. Rev*. **2012**, *112*, 5317–5338.
9. Kundu, M.; Krishnan, P.; Kotnala, R.K.; et al. Recent developments in biosensors to combat agricultural challenges and their future prospects. *Trends Food Sci. Technol*. **2019**, *88*, 157–178.
10. Fang, Y.; Ramasamy, R.P. Current and prospective methods for plant disease detection. *Biosensors* **2015**, *5*, 537–561.
11. Bakker, E.; Qin, Y. Electrochemical sensors. *Anal. Chem.* **2006**, *78*, 3965–3984.
12. Singh, P.; Kamble, G.S.; Ghodake, G.K.; et al. A Newly Emerging Trend of Chitosan-Based Sensing Platform for the Organophosphate Pesticide Detection Using Acetylcholinesterase: A Review. *Trends Food Sci. Technol.* **2019**, *85*, 78–91.
13. Sgobbi, L.F.; Machado, S.A.S. Functionalized polyacrylamide as an acetylcholinesterase-inspired biomimetic device for electrochemical sensing of organophosphorus pesticides. *Biosens. Bioelectron.* **2018**, *100*, 290–297.
14. Ristori, C.; Del Carlo, C.; Martini, M.; et al. Potentiometric detection of pesticides in water samples. *Anal. Chim. Acta* **1996**, *325*, 151–160.
15. Cabral, M.F.; Sgobbi, L.F.; Kataoka, E.M.; et al. On the behavior of acetylcholinesterase immobilized on carbon nanotubes in the presence of inhibitors. *Colloids Surf. B* **2013**, *111*, 30–35.
16. Sgobbi, L.F.; Zibordi-Besse, L.; Rodrigues, B.V.M.; et al. Polyhydroxamicalkanoate as a bioinspired acetylcholinesterase-based catalyst for acetylthiocholine hydrolysis and organophosphorus dephosphorylation: Experimental studies and theoretical insights. *Catal. Sci. Technol.* **2017**, *7*, 3388–3398.
17. Teixeira, S.C.; Gomes, N.O.; Calegaro, M.L.; et al. Sustainable plant-wearable sensors for on-site, rapid decentralized detection of pesticides toward precision agriculture and food safety. *Biomater. Adv.* **2023**, *155*, 213676–213686.
18. Caetano, J.; Machado, S.A.S. Determination of carbaryl in tomato in natura using an amperometric biosensor based on the inhibition of acetylcholinesterase activity. *Sens. Actuators B* **2008**, *129*, 40–46.
19. Patel, H.; Rawtani, D.; Agrawal, Y.K. A newly emerging trend of chitosan-based sensing platform for the organophosphate pesticide detection using acetylcholinesterase—A review. *Trends Food Sci. Technol.* **2019**, *85*, 78–91.
20. Periasamy, A.P.; Umasankar, Y.; Chen, S.-M. Nanomaterials–acetylcholinesterase enzyme matrices for organophosphorus pesticides electrochemical sensors: A review. *Sensors* **2009**, *9*, 4034–4055.
21. Zhu, C.; Yang, G.; Li, H.; et al. Electrochemical sensors and biosensors based on nanomaterials and nanostructures. *Anal. Chem.* **2015**, *87*, 230–249.
22. Wang, J. Nanomaterial-based electrochemical biosensors. *Analyst* **2005**, *130*, 421–426.
23. Pumera, M.; Sanchez, S.; Ichinose, I.; et al. Electrochemical nanobiosensors. *Sens. Actuators B* **2007**, *123*, 1195–1205.
24. Du, D.; Chen, S.; Cai, J.; et al. Immobilization of acetylcholinesterase on gold nanoparticles embedded in sol–gel film for amperometric detection of organophosphorous insecticide. *Biosens. Bioelectron.* **2007**, *23*, 130–134.
25. Castro, F.L.; Castro, A.C.H.; Silva, M.R.A.; et al. Electrochemical detection of SARS-CoV-2 in saliva using ZnO nanorods functionalized with gold-conjugated anti-RBD antibodies. *ChemNanoMat* **2025**, *12*, e202500411.
26. Sabaine, A.E.; Castro, A.C.H.; Mancini, R.S.N.; et al. Peptide-based biosensors for variant-specific detection of SARS-CoV-2 antibodies. *Mater. Adv.* **2025**, *6*, 7090–7103.
27. Nicoliche, C.Y.N.; Pascon, A.M.; Bezerra, Í.R. S.; et al. In situ nanocoating on porous pyrolyzed paper enables antibiofouling and sensitive electrochemical analyses in biological fluids. *ACS Appl. Mater. Interfaces* **2022**, *14*, 2522–2533.

28. Liu, G.; Wang, J.; Barry, R.; et al. Nanoparticle-based electrochemical immunosensor for the detection of phosphorylated acetylcholinesterase: An exposure biomarker of organophosphate pesticides and nerve agents. *Chem. Eur. J.* **2008**, *14*, 9951–9959.
29. Du, D.; Ding, J.; Cai, J.; et al. Electrochemical thiocholine inhibition sensor based on biocatalytic growth of Au nanoparticles using chitosan as template. *Sens. Actuators B* **2007**, *127*, 317–322.
30. Du, D.; Chen, S.; Song, D.; et al. Development of acetylcholinesterase biosensor based on CdTe quantum dots/gold nanoparticles modified chitosan microspheres interface. *Biosens. Bioelectron.* **2008**, *24*, 475–479.
31. Gong, J.; Wang, L.; Zhang, L. Electrochemical biosensing of methyl parathion pesticide based on acetylcholinesterase immobilized onto Au–polypyrrole interlaced network-like nanocomposite. *Biosens. Bioelectron.* **2009**, *24*, 2285–2288.
32. Alves, W.A.; Pelin, J.N.B.D.; Edwards-Gayle, C.J.C.; et al. Self-assembled gold nanoparticles and amphiphile peptides: A colorimetric probe for copper(II) ion detection. *Dalton Trans.* **2020**, *49*, 16226–16237.
33. Gerbelli, B.B.; Vassilaides, S.V.; Rojas, J.E.U.; et al. Hierarchical self-assembly of peptides and its applications in bionanotechnology. *Macromol. Chem. Phys.* **2019**, *220*, 1900085.
34. Pelin, J.N.B.D.; Gatto, E.; Venanzi, M.; et al. Hybrid conjugates formed between gold nanoparticles and an amyloidogenic diphenylalanine-cysteine peptide. *ChemistrySelect* **2018**, *3*, 6756–6765.
35. Karpel, R.L.; Liberato, M.S.; Campeiro, J.D.; et al. Design and characterization of crotamine-functionalized gold nanoparticles. *Colloids Surf. B* **2018**, *163*, 1–8.
36. Wang, S.S. p-Alkoxybenzyl alcohol resin and p-alkoxybenzyloxycarbonylhydrazide resin for solid-phase synthesis of protected peptide fragments. *J. Am. Chem. Soc.* **1973**, *95*, 1328–1333.
37. Turkevich, J.; Stevenson, P.C.; Hillier, J. A study of the nucleation and growth processes in the synthesis of colloidal gold. *Discuss. Faraday Soc.* **1951**, *11*, 55–75.
38. Laviron, E. General expression of the linear potential sweep voltammogram in the case of diffusionless electrochemical systems. *J. Electroanal. Chem.* **1979**, *101*, 19–28.
39. Wessler, I.; Michel-Schmidt, R.; Kirkpatrick, C.J. pH-dependent hydrolysis of acetylcholine: Consequences for non-neuronal acetylcholine. *Int. Immunopharmacol.* **2015**, *29*, 27–30.
40. Štěpánek, P. Data analysis in dynamic light scattering. In *Dynamic Light Scattering*; Oxford University Press: Oxford, UK, 2023.
41. Hunter, R.J. *Zeta Potential in Colloid Science: Principles and Applications*; Academic Press: London, UK, 1981.
42. Hackley, V.A.; Premachandran, R.S.; Malghan, S.G.; et al. A standard reference material for the measurement of particle mobility by electrophoretic light scattering. *Colloids Surf. A* **1995**, *98*, 195–203.
43. Carone, A.; Emilsson, S.; Mariani, P.; et al. Gold nanoparticle shape dependence of colloidal stability domains. *Nanoscale Adv.* **2023**, *5*, 2017–2026.
44. Väli, R.; Jänes, A.; Lust, E. Alkali-metal insertion processes on nanospheric hard carbon electrodes: An electrochemical impedance spectroscopy study. *J. Electrochem. Soc.* **2017**, *164*, E3429–E3436.
45. Phongphut, A.; Chayasombat, B.; Cass, A.E.; et al. Biosensors based on acetylcholinesterase immobilized on clay–gold nanocomposites for the discrimination of chlorpyrifos and carbaryl. *ACS Omega* **2022**, *7*, 39848–39859.
46. Nunes, E.W.; Silva, M.K.; Rascón, J.; et al. Acetylcholinesterase biosensor based on functionalized renewable carbon platform for detection of carbaryl in food. *Biosensors* **2022**, *12*, 486.
47. Pohanka, M. Electrochemical biosensors based on acetylcholinesterase and butyrylcholinesterase: A review. *Int. J. Electrochem. Sci.* **2016**, *11*, 7440–7452.
48. Tun, W.S.T.; Saenchoopa, A.; Daduang, S.; et al. Electrochemical biosensor based on cellulose nanofibers/graphene oxide and acetylcholinesterase for the detection of chlorpyrifos pesticide in water and fruit juice. *RSC Adv.* **2023**, *13*, 9603–9614.
49. Wang, B.; Li, Y.; Hu, H.; et al. Acetylcholinesterase electrochemical biosensors with graphene-transition metal carbides nanocomposites modified for detection of organophosphate pesticides. *PLoS ONE* **2020**, *15*, e0231981.
50. Hart, J.P.; Hartley, I.C. Voltammetric and amperometric studies of thiocholine at a screen-printed carbon electrode chemically modified with cobalt phthalocyanine: Studies towards a pesticide sensor. *Analyst* **1994**, *119*, 259–263.
51. Oliveira, A.C.; Mascaro, L.H. Evaluation of acetylcholinesterase biosensor based on carbon nanotube paste in the determination of chlorphenvinphos. *Int. J. Anal. Chem.* **2011**, *2011*, 974216.
52. Sucheta, A.; Cammack, R.; Weiner, J.; et al. Reversible electrochemistry of fumarate reductase immobilized on an electrode surface: Direct voltammetric observations of redox centers and their participation in rapid catalytic electron transport. *Biochemistry* **1993**, *32*, 5455–5465.
53. Liu, Q.; Fei, A.; Huan, J.; et al. Effective amperometric biosensor for carbaryl detection based on covalent immobilization of acetylcholinesterase on multiwall carbon nanotubes/graphene oxide nanoribbons nanostructure. *J. Electroanal. Chem.* **2015**, *740*, 8–13.
54. Badawy, M.E.I.; El-Aswad, A.F. Bioactive paper sensor based on acetylcholinesterase for the rapid detection of organophosphate and carbamate pesticides. *Int. J. Anal. Chem.* **2014**, *2014*, 536823.

55. Timur, S.; Telefoncu, A. Acetylcholinesterase (AChE) electrodes based on gelatin and chitosan matrices for pesticide detection. *Artif. Cells Blood Substit. Biotechnol.* **2004**, *32*, 427–442.
56. Zhang, Y.; Liu, H.; Yang, Z.; et al. An acetylcholinesterase inhibition biosensor based on a reduced graphene oxide/silver nanocluster/chitosan nanocomposite for detection of organophosphorus pesticides. *Anal. Methods* **2015**, *7*, 6213–6219.
57. Gong, J.; Liu, T.; Song, D.; et al. One-step fabrication of three-dimensional porous calcium carbonate–chitosan composite film as the immobilization matrix of acetylcholinesterase and its biosensing on pesticide. *Electrochem. Commun.* **2009**, *11*, 1873–1876.
58. Cui, H.-F.; Wu, W.-W.; Li, M.-M.; et al. A highly stable acetylcholinesterase biosensor based on chitosan–TiO_2–graphene nanocomposites for detection of organophosphate pesticides. *Biosens. Bioelectron.* **2018**, *99*, 223–229.
59. Song, D.; Li, Y.; Lu, X.; et al. Palladium–copper nanowires-based biosensor for the ultrasensitive detection of organophosphate pesticides. *Anal. Chim. Acta* **2017**, *982*, 168–175.
60. Zhao, H.; Ji, X.; Wang, B.; et al. An ultra-sensitive acetylcholinesterase biosensor based on reduced graphene oxide–Au nanoparticles–β-cyclodextrin/Prussian blue–chitosan nanocomposites for organophosphorus pesticides detection. *Biosens. Bioelectron.* **2015**, *65*, 23–30.
61. Nesakumar, N.; Ramachandra, B.L.; Sethuraman, S.; et al. Evaluation of inhibition efficiency for the detection of captan, 2,3,7,8-tetrachlorodibenzodioxin, pentachlorophenol, and carbosulfan in water: An electrochemical approach. *Bull. Environ. Contam. Toxicol.* **2016**, *96*, 217–223.
62. Guo, Y.; Sun, X.; Liu, X.; et al. A miniaturized portable instrument for rapid determination of pesticide residues in vegetables and fruits. *IEEE Sens. J.* **2015**, *15*, 4046–4052.
63. Du, D.; Huang, X.; Cai, J.; et al. Comparison of pesticide sensitivity by electrochemical test based on acetylcholinesterase biosensor. *Biosens. Bioelectron.* **2007**, *23*, 285–289.
64. Du, D.; Ding, J.; Tao, Y.; et al. Application of chemisorption/desorption process of thiocholine for pesticide detection based on acetylcholinesterase biosensor. *Sens. Actuators B* **2008**, *134*, 908–912.
65. Sun, X.; Wang, X. Acetylcholinesterase biosensor based on Prussian blue–modified electrode for detecting organophosphorous pesticides. *Biosens. Bioelectron.* **2010**, *25*, 2611–2614.
66. Yan, J.; Guan, H.; Yu, J.; et al. Acetylcholinesterase biosensor based on assembly of multiwall carbon nanotubes onto liposome bioreactors for detection of organophosphate pesticides. *Pestic. Biochem. Physiol.* **2013**, *105*, 197–202.
67. Guan, H.; Zhang, F.; Yu, J.; et al. Novel acetylcholinesterase biosensors based on liposome bioreactors–chitosan nanocomposite film for detection of organophosphate pesticides. *Food Res. Int.* **2012**, *49*, 15–21.
68. Sun, X.; Li, Q.; Wang, X. AChE biosensor based on aniline–MWNTs modified electrode for the detection of pesticides. In Proceedings of the 2011 IEEE/ICME International Conference on Complex Medical Engineering, Harbin, China, 22–25 May 2011; pp 441–444.
69. Zhao, Y.; Zhang, S.P.; Ma, J.; et al. Determination of carbamate pesticide methomyl using acetylcholinesterase/MWNTs–chitosan modified glassy carbon electrode. *Int. J. Electrochem. Sci.* **2012**, *7*, 8856–8867.
70. Dong, J.; Zhao, H.; Qiao, F.; et al. Quantum dot immobilized acetylcholinesterase for the determination of organophosphate pesticides using graphene–chitosan nanocomposite modified electrode. *Anal. Methods* **2013**, *5*, 2866–2872.
71. Du, D.; Wang, M.; Cai, J.; et all. One-step synthesis of multiwalled carbon nanotubes–gold nanocomposites for fabricating amperometric acetylcholinesterase biosensor. *Sens. Actuators B* **2010**, *143*, 524–529.
72. Zhai, C.; Sun, X.; Zhao, W.; et al. Acetylcholinesterase biosensor based on chitosan/Prussian blue/multiwall carbon nanotubes/hollow gold nanospheres nanocomposite film by one-step electrodeposition. *Biosens. Bioelectron.* **2013**, *42*, 124–130.
73. Kandimalla, V.B.; Ju, H. Binding of acetylcholinesterase to multiwall carbon nanotube–cross-linked chitosan composite for flow-injection amperometric detection of an organophosphorous insecticide. *Chem. Eur. J.* **2006**, *12*, 1074–1080.
74. El-Moghazy, A.Y.; Soliman, E.A.; Ibrahim, H.Z.; et al. Biosensor based on electrospun blended chitosan–poly(vinyl alcohol) nanofibrous enzymatically sensitized membranes for pirimiphos-methyl detection in olive oil. *Talanta* **2016**, *155*, 258–264.
75. Talarico, D.; Arduini, F.; Amine, A.; et al. Screen-printed electrode modified with carbon black and chitosan: A novel platform for acetylcholinesterase biosensor development. *Anal. Bioanal. Chem.* **2016**, *408*, 7299–7309.
76. Du, D.; Ding, J.; Cai, J.; et al. One-step electrochemically deposited interface of chitosan–gold nanoparticles for acetylcholinesterase biosensor design. *J. Electroanal. Chem.* **2007**, *605*, 53–60.
77. Yang, Y.; Guo, M.; Yang, M.; et al. Determination of pesticides in vegetable samples using an acetylcholinesterase biosensor based on nanoparticles ZrO_2/chitosan composite film. *Int. J. Environ. Anal. Chem.* **2005**, *85*, 163–175.
78. Liu, T.; Su, H.; Qu, X.; et al. Acetylcholinesterase biosensor based on 3-carboxyphenylboronic acid/reduced graphene oxide–gold nanocomposites modified electrode for amperometric detection of organophosphorus and carbamate pesticides. *Sens. Actuators B* **2011**, *160*, 1255–1261.